natureresearch
https://doi.org/10.1038/s41563-020-0798-1

Supplementary information

Mechanically robust lattices inspired by deep-sea glass sponges

In the format provided by the authors and unedited

Supplementary Information: Mechanically Robust Lattices Inspired By Deep-Sea Glass Sponges

MATHEUS C. FERNANDES[1,2], JOANNA AIZENBERG[1,2,3], JAMES C. WEAVER[1,2,†], AND KATIA BERTOLDI[1,2,3,‡]

[1] *John A. Paulson School of Engineering and Applied Sciences – Harvard University, Cambridge, MA 02138*
[2] *Wyss Institute – Harvard University, Cambridge, MA 02138*
[3] *Kavli Institute – Harvard University, Cambridge, MA 02138*
Corresponding authors: [†] *jweaver@seas.harvard.edu*,[‡] *bertoldi@seas.harvard.edu*

S1: STRUCTURE OF THE HEXACTINELLID SPONGE *EUPLECTELLA ASPERGILLUM*

The periodic structures investigated in this study are inspired by the skeleton of the hexactinellid sponge *Euplectella aspergillum*, which throughout its lifespan (Supplementary Fig. 1) progresses from a easily deformable skeletal lattice (flexible phase), consisting of loosely associated individual skeletal elements, through various stages of skeletal consolidation, ultimately resulting in the mature form (rigid phase), shown in Main Text Fig. 1[S1–S3]. In this section, we provide a detailed description of the sponge's geometry and measured dimensions.

Main Text Fig 1. shows a photograph of the entire skeleton of a representative specimen of *E. aspergillum*, and its intricate, cylindrical cage-like structure (20 to 25 cm long, 2 to 4 cm in diameter)[S4]. The surface of the cylinder incorporates a regular square lattice composed of a series of cemented vertical and horizontal struts, consisting of bundles of individual spicules, each with a circular cross-section. The cell spacing between horizontal and vertical struts is $L \approx 2.5$ mm[S5], while the diameter is $D_{nd} \approx 0.25$ mm[S5]. In addition to the horizontal and vertical struts, there is an additional set of diagonal elements, intersecting in a manner that creates a series of alternating open and closed cells, reminiscent of a checkerboard pattern[S5]. Although these diagonal elements are not as ordered as the horizontal and vertical ones, they can be approximated as two diagonal struts that are offset from the nodes (vertex joints between non-diagonal elements) and form roughly octagonal openings (Supplementary Fig. 2). To estimate the volume ratio between diagonal and non-diagonal elements, we acquired digital photographs of the sponge skeleton and performed image segmentation to segregate the projected area of the vertical/horizontal and diagonal spicules. For these measurements, and to minimize shadowing artifacts during image thresholding, sponge skeleton regions were selected that did not contain surface ridges. In total 4 different sponge skeletons were investigated and 25 different lattice cells from each specimen were analyzed. Using this approach, the projected area ratio of non-diagonal to diagonal elements was found to be $A_{nd}/A_d \approx 1.41 \pm 0.16$. Note that here, and in the following, the subscripts d and nd are used to indicate the diagonal and non-diagonal (i.e. horizontal and vertical) elements, respectively.

Finally, it should also be noted that the sponge is reinforced by external ridges that extend perpendicular to the surface of the cylinder and spiral the cage at an angle of $\sim 45^{\circ}$. However, in this paper we do not report the effects of these ridges on its mechanical performance, which will be addressed elsewhere.

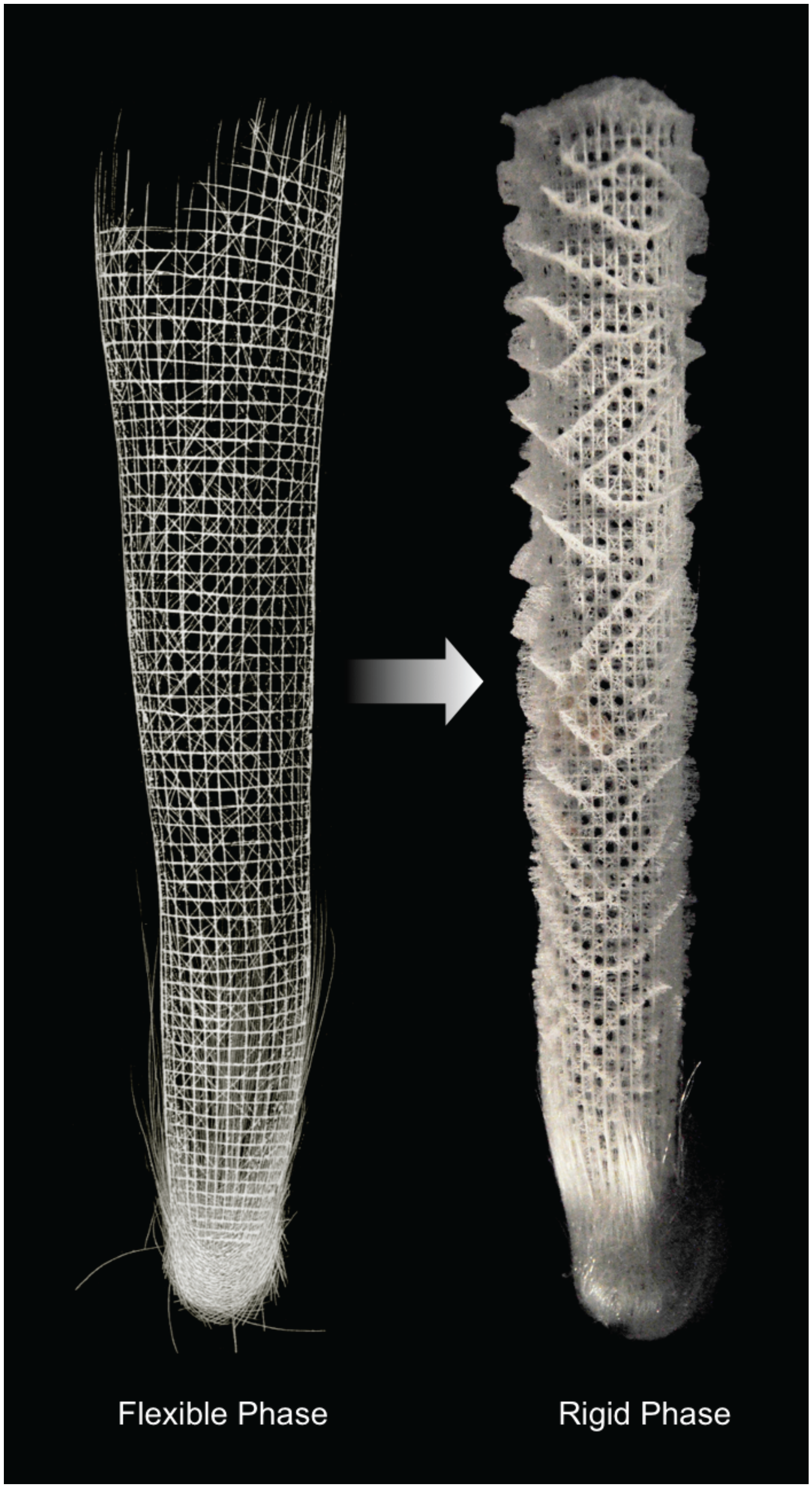

Supplementary Figure 1: Historical illustration (left) and modern photograph (right) illustrating the flexible and rigid growth stages that occur during skeletal maturation in several hexactinellid sponges in the genus *Euplectella*. Left image adapted from Schulze[S2].

S2: OUR FOUR LATTICE DESIGNS

In this study, we focused on four different lattice configurations (*Designs A, B, C*, and *D*) constrained to deform in an in-plane setting only. In an effort to conduct a fair performance comparison between the different geometries, all four lattices were designed to contain the same total volume of material and a fixed volume ratio between non-diagonal and diagonal elements (chosen to match the sponge geometry) for *Designs A, B*, and *C*. Two different shapes were considered for the cross-section of the struts: circular and rectangular. For the circular cross-section case, we denoted the diameters of the non-diagonal (i.e. horizontal and vertical) and diagonal struts in the α-th design as $D_{\alpha,nd}$ and $D_{\alpha,d}$, respectively, and neglected out-of-plane buckling. For the rectangular cross-sections, we denoted the in-plane thickness of the non-diagonal (i.e. horizontal and vertical) and diagonal struts in the α-th design as $T_{\alpha,nd}$ and $T_{\alpha,d}$, respectively, and chose the depth H to avoid out-of-plane deformation (i.e. we chose the depth over thickness ratio sufficiently large to constrain in-plane deformation). Finally, it is important to note that the slenderness of the non-diagonal members in the α-th design $\in [A, B, C]$ was chosen as

$$\frac{D_{\alpha,nd}}{L} = 0.1, \quad \text{and} \quad \frac{T_{\alpha,nd}}{L} = 0.1, \tag{1}$$

for the case of the circular and rectangular cross-section, since this was the aspect ratio measured for the sponges (Section S1).

In the subsequent sections, we describe in detail the unit cells for four different designs, and provide the derivations for the characteristics of each geometry cross-section. To derive these relations, we laid a framework of underlying assumptions, namely:

- in-plane geometry is uniform and has the same shape (allowing only either thickness or diameter to change depending on cross-sectional shape) for all elements,
- all diagonal elements have the same in-plane dimension,
- all non-diagonal elements have the same in-plane dimension, and
- area of overlapping beam crossing is negligible and unaccounted for during volume calculations.

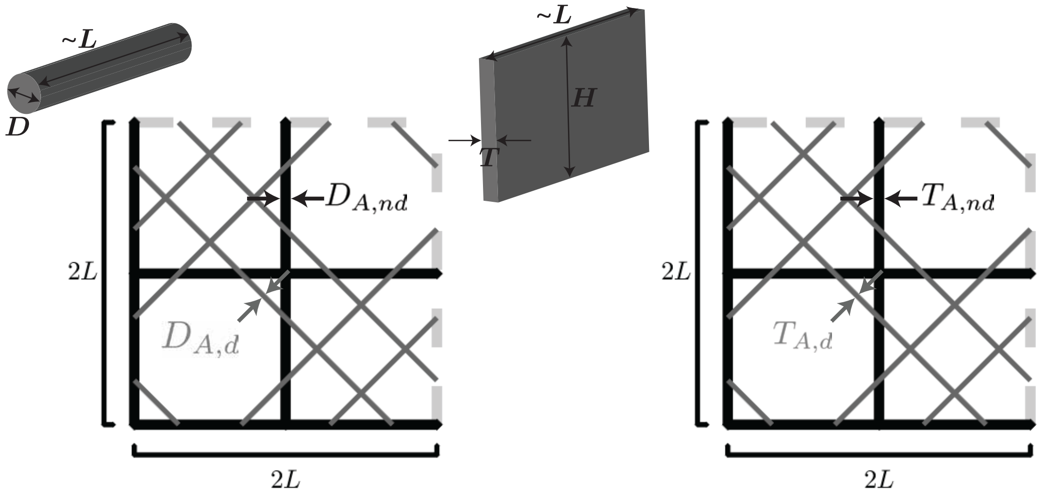

Supplementary Figure 2: **Unit cell for *Design A*.** Schematics of the unit cell for *Design A* (the sponge-inspired lattice). On the left, we indicate the geometric parameters of this design considering a circular cross-section, while on the right, we show the geometric parameters of this design considering a rectangular cross-section.

S2.1: Design A

Design A was inspired by the sponge's skeletal architecture and consisted of a square grid reinforced by a double diagonal support system (Supplementary Fig. 2). Matching what was seen in the natural sponge, the diagonal elements were assumed to form an octagonal opening on every other cell, such that they intersect the horizontal and vertical struts at a distance $\Delta L = L/(\sqrt{2}+2)$ from the nodes, where L denotes the length of the vertical and horizontal struts.

S2.1.1: Circular cross-section

Assuming that the cross-section of all struts is circular, the projected area and volume for the non-diagonal ($A_{A,nd}$ and $V_{A,nd}$) and diagonal ($A_{A,d}$ and $V_{A,d}$) members are given by

$$A_{A,nd} = 8LD_{A,nd}, \tag{2}$$

$$V_{A,nd} = 8L\left(\pi\frac{D_{A,nd}^2}{4}\right) = 2L\pi D_{A,nd}^2 \tag{3}$$

$$A_{A,d} = 8\sqrt{2}LD_{A,d}, \tag{4}$$

and

$$V_{A,d} = 8\sqrt{2}L\left(\pi\frac{D_{A,d}^2}{4}\right) = 2\sqrt{2}L\pi D_{A,d}^2. \tag{5}$$

Since the projected area ratio of the non-diagonal to diagonal elements in the sponge has been measured to be

$$\frac{A_{A,nd}}{A_{A,d}} = 1.41, \tag{6}$$

by substituting Eq. (2) and Eq. (4) into the equation above we find that for *Design A*

$$D_{A,nd} = 1.41\sqrt{2}D_{A,d} \approx 2D_{A,d}. \tag{7}$$

Substitution of Eq. (7) into Eq. (3) and Eq. (5) yields

$$\frac{V_{A,nd}}{V_{A,d}} = \frac{2L\pi D_{A,nd}^2}{2\sqrt{2}L\pi D_{A,d}^2} = 2\sqrt{2} \tag{8}$$

and

$$V_{A,T} = V_{A,nd} + V_{A,d} = 2\pi L(D_{A,nd}^2 + \sqrt{2}D_{A,d}^2) = 2\pi L D_{A,nd}^2\left(1 + \frac{1}{2\sqrt{2}}\right), \tag{9}$$

where $V_{A,T}$ indicates the total volume of the unit cell for *Design A*.

Finally, it is important to note that in this study we used *Design A* as our base model, and thus constrained the total volume of all the other unit cell designs with circular cross-sections to be equal to that of *Design A*, namely,

$$V_{\alpha,d} + V_{\alpha,nd} = V_{A,T} = 2\pi L D_{A,nd}^2\left(1 + \frac{1}{2\sqrt{2}}\right), \tag{10}$$

with $\alpha =$ B, C and D. For *Designs B* and *C*, which comprised diagonal elements, we also constrained the volume ratio of the non-diagonal to diagonal elements to be the same as in *Design A*

$$\frac{V_{\alpha,nd}}{V_{\alpha,d}} = \frac{V_{A,nd}}{V_{A,d}} = 2\sqrt{2}, \tag{11}$$

with $\alpha \in$ B and C.

S2.1.2: Rectangular cross-section

Assuming that the cross-section of all struts is rectangular, the projected-area for the non-diagonal ($A_{A,nd}$) and diagonal ($A_{A,d}$) members is given by

$$A_{A,nd} = 8LT_{A,nd} \tag{12}$$

and

$$A_{A,d} = 8\sqrt{2}LT_{A,d} \tag{13}$$

where $T_{A,nd}$ and $T_{A,d}$ are the non-diagonal and diagonal in-plane strut thickness for *Design A*, respectively. Since for the sponge $A_{nd}/A_d \approx 1.41$, it follows that

$$T_{A,nd} = 2T_{A,d}. \tag{14}$$

Finally, for the case of rectangular cross-section we used *Design A* as our base model, and thus constrained the total volume of all the other unit cell designs with rectangular cross-section to be equal to that of *Design A*, namely,

$$V_{A,T} = V_{\alpha,d} + V_{\alpha,nd} = 8LH(T_{A,nd} + \sqrt{2}T_{A,d}) = 8LHT_{A,nd}\left(1 + \frac{1}{\sqrt{2}}\right), \tag{15}$$

with $\alpha \in$ B, C and D. Moreover, for *Designs B-C*, which comprised diagonal elements, we also constrained the volume ratio of the non-diagonal to diagonal elements to be the same as in *Design A*,

$$\frac{V_{\alpha,nd}}{V_{\alpha,d}} = \sqrt{2}, \tag{16}$$

with $\alpha \in$ B and C.

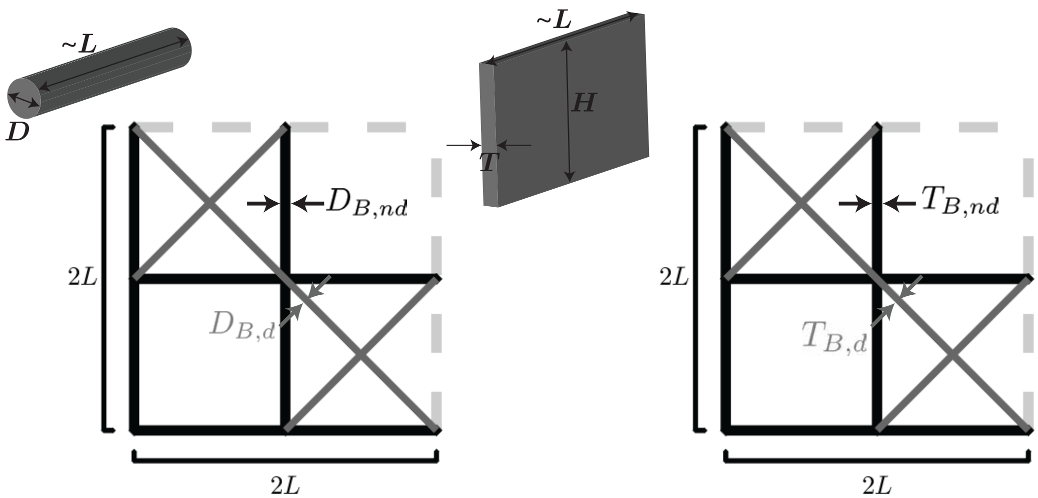

Supplementary Figure 3: Unit cell for *Design B*. Schematics of the unit cell for *Design B* (an alternating open and closed cell structure resembling the sponge and employing a single set of diagonal bracings). On the left we indicate the geometric parameters of this design considering a circular cross-section, while on the right we show the geometric parameters of this design considering a rectangular cross-section.

S2.2: Design B

Design B was similar to the sponge design (*Design A*) and was likewise characterized by an alternation of open and closed cells (Supplementary Fig. 3). However, instead of having two diagonals offset from the nodes, in this design only one diagonal passes through the nodes crossing though every other cell.

S2.2.1: Circular cross-section

For this design with circular cross-section, the non-diagonal and diagonal volumes are given by

$$V_{B,nd} = V_{A,nd} = 2\pi LD^2_{B,nd} \tag{17}$$

and

$$V_{B,d} = 2\sqrt{8}L\left(\pi\frac{D^2_{B,d}}{4}\right), \tag{18}$$

respectively. Using the constraints provided by Eq. (10) and Eq. (11), as well as the above volumes, we obtain

$$D_{B,nd} = D_{A,nd} \tag{19}$$

and

$$\frac{D_{B,d}}{D_{B,nd}} = \frac{1}{\sqrt{2}}. \tag{20}$$

S2.2.2: Rectangular cross-section

For this design with circular cross-section, the volume of the non-diagonal and diagonal members are given by

$$V_{B,nd} = 8LT_{B,nd}H. \tag{21}$$

and

$$V_{B,d} = 4\sqrt{2}LT_{B,d}H. \tag{22}$$

Using the constraints provided by Eq. (15) and Eq. (16), as well as the above volumes, we obtain

$$T_{B,nd} = T_{B,d} \tag{23}$$

and

$$T_{B,nd} = T_{A,nd} \tag{24}$$

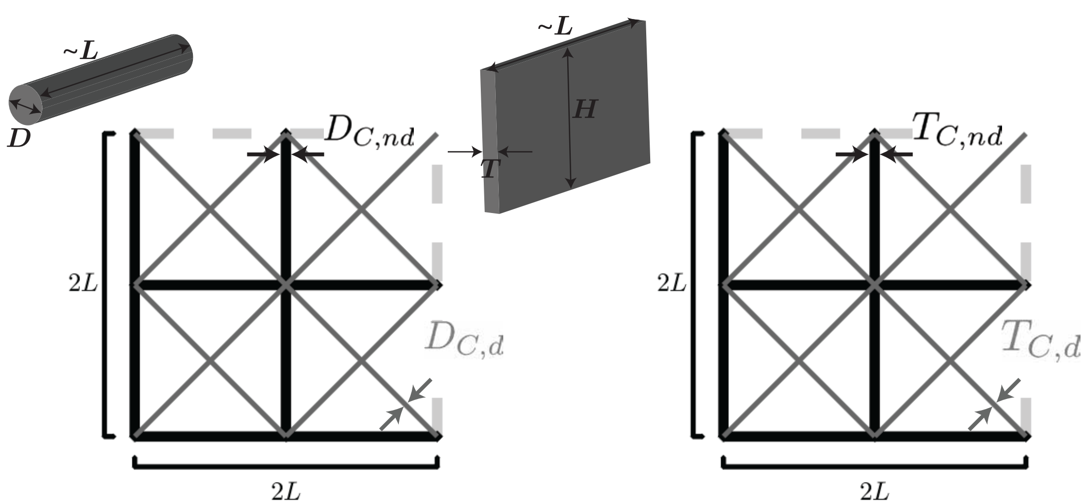

Supplementary Figure 4: Unit cell for *Design C*. Schematics of the unit cell for *Design C* (all cells filled with diagonal bracings, as is typically found in infrastructure applications). On the left we indicate the geometric parameters of this design considering a circular cross-section, while on the right we show the geometric parameters of this design considering a rectangular cross-section.

S2.3: Design C

Design C was inspired by the Town lattice truss design introduced by architect Ithiel Town in 1820[S6] and consisted of every cell being reinforced by diagonal trusses passing through the nodes (Supplementary Fig. 4).

S2.3.1: Circular cross-section

For this design with circular cross-section, the volume of the non-diagonal and diagonal members of the unit cell are given by

$$V_{C,nd} = V_{A,nd} = 2L\pi D_{A,nd}^2 \tag{25}$$

and

$$V_{C,d} = V_{A,d} = 2\sqrt{2}L\pi D_{A,d}^2, \tag{26}$$

respectively. Using the constraints provided by Eq. (10) and Eq. (11) we obtain

$$D_{C,nd} = D_{A,nd} \tag{27}$$

and

$$\frac{D_{C,d}}{D_{C,nd}} = \frac{1}{2}. \tag{28}$$

S2.3.2: Rectangular cross-section

For this design with circular cross-section, the volume of the non-diagonal and diagonal members of the unit cell are given by

$$V_{C,nd} = 8LT_{C,nd}H \tag{29}$$

and

$$V_{C,d} = 8\sqrt{2}LT_{C,d}H \tag{30}$$

Using the constraints provided by Eq. (15) and Eq. (16), as well as the above volumes, we obtain

$$T_{C,nd} = 2T_{C,d}, \tag{31}$$

and

$$T_{C,nd} = T_{A,nd}. \tag{32}$$

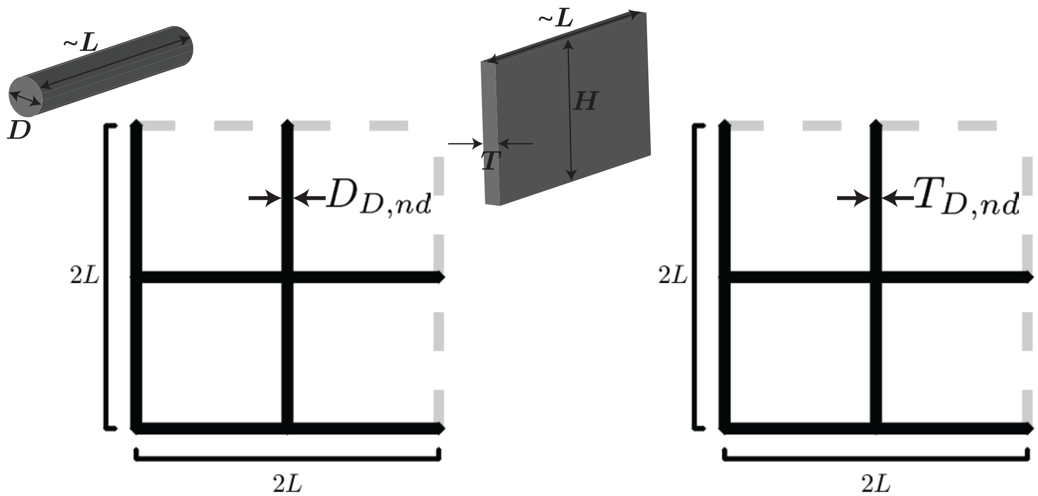

Supplementary Figure 5: Unit cell for *Design D*. Schematics of the unit cell for *Design D* (square lattice with no diagonal reinforcement). On the left we indicate the geometric parameters of this design considering a circular cross-section, while on the right we show the geometric parameters of this design considering a rectangular cross-section.

S2.4: Design D

Design D comprised only the square grid without diagonal reinforcement (Supplementary Fig. 5). As such, for this design we allocated the total material volume to the non-diagonal elements. Note that this design is well known to be unstable and very limited in resisting shear forces[S7,S8].

S2.4.1: Circular cross-section

Since

$$V_{D,T} = V_{D,nd} = V_{A,nd} = 2\pi L D_{D,nd}^2, \tag{33}$$

using the constraint provided by Eq. (10) we obtain

$$D_{D,nd} = D_{A,nd}\sqrt{1+\frac{\sqrt{2}}{4}}. \tag{34}$$

S2.4.2: Rectangular cross-section

Since

$$V_{D,T} = V_{D,nd} = 8LT_{D,nd}H, \tag{35}$$

using the constraint provided by Eq. (15) we obtain

$$T_{D,nd} = \left(1+\frac{1}{\sqrt{2}}\right)T_{A,nd} \tag{36}$$

S3: EXPERIMENTAL SETUP

S3.1: Fabrication

We fabricated each of the lattice specimens with a Stratasys Connex500 multi-material 3D printer using the digital material FLX9795-DM. During the fabrication process, a photosensitive liquid precursor (the 3D printer "ink") is deposited in a voxel-by-voxel fashion. Several precursors are used to print multiple materials with different properties and the resulting modulus can be tuned by varying the concentration of photo-initiator. A UV light cross-links the liquid precursors in a layer-by-layer fashion and this process is repeated until the full 3D model is built. Each of the specimens were printed in parallel along with the print-head direction as to minimize material anisotropy between specimens. Depending on the liquid precursor composition and the degree of cross-linking, a broad range of mechanical properties can be achieved from stiff thermoplastic-like to soft rubber-like materials. For the samples fabricated for this study, we tuned the process to realize a material with an initial shear modulus $\mu = 14.5$ MPa. The dimensions of the fabricated samples (as measured with a caliper) are shown in Supplementary Tab. 1, and all fabricated lattices had depth (through thickness) $H = 40$ mm.

S3.2: Testing

All samples were tested using an Instron 5969 with a compression speed of 0.2 mm/min in order to allow material viscoelastic relaxation, thus achieving the material's fully elastic behavior. Note that the specific compression speed was determined by testing similar structures at different loading rates until the stress-strain curve achieved a rate independent solution.

To test the response of the specimens under uniaxial compression, we used standard compression plates with a 50kN load cell. The response under bending was also characterized using a 3-point bend test mount and a 500N load cell. While similar results were obtained regardless of whether the models were loaded parallel or perpendicular to the print direction, for experimental consistency all tests were performed with models oriented parallel to the print direction.

	Design A	**Design B**	**Design C**	**Design D**	**Optimal Design**
Total Length (Test Dir.) [mm]	93.29 [93]	93.45 [93]	93.47 [93]	93.25 [93]	93.27 [93]
Total Length (Non-Test Dir.) [mm]	93.52 [93]	93.31[93]	93.55 [93]	93.19 [93]	93.54 [93]
Depth H [mm]	39.98 [40]	40.06 [40]	40.19 [40]	40.10 [40]	40.25 [40]
Top L [mm]	14.7 [15]	14.95 [15]	14.93 [15]	14.96 [15]	15.02 [15]
Top $T_{\alpha,nd}$ [mm]	1.48 [1.5]	1.56 [1.5]	1.51 [1.5]	2.68 [2.56]	1.11 [1.03]
Top $T_{\alpha,d}$ [mm]	0.86 [0.75]	1.53 [1.5]	0.78 [0.75]	N/A	1.07 [1.08]
Bottom L [mm]	15.04 [15]	15.01 [15]	15.01 [15]	14.96 [15]	15.05 [15]
Bottom $T_{\alpha,nd}$ [mm]	1.55 [1.5]	1.57 [1.5]	1.57 [1.5]	2.69 [2.56]	1.11 [1.03]
Bottom $T_{\alpha,d}$ [mm]	0.85 [0.75]	1.61 [1.5]	0.86 [0.75]	N/A	1.08 [1.08]
Weight [g]	145.2	148.4	150.8	143.36	146.36

Supplementary Table 1: 3D Printed Model Caliper Sample Measurements. This table provides the caliper measurements averaged over $n = 3$ separate specimens for each design (values in black) as well as the expected values (bracketed values in red). All measurements reported were conducted prior to testing the samples.

S4: FINITE ELEMENT (FE) ANALYSIS

The finite element analyses presented in this article were conducted using *ABAQUS/Standard*. All models were constructed using 1D Timoshenko beam elements (ABAQUS element type B22) and all beam crossings were assumed to be welded joints. For each instance, seeding of the mesh was chosen to be at least 1/10 of the minimum beam length. The response of the material was captured using an incompressible Neo-Hookean material model with shear modulus $\mu = 14.5$ MPa. Due to small inconsistencies in the 3D printing process (Supplementary Tab. 1), we adjusted the dimensions of the FE models accordingly by applying a mass correction based on data derived from the 3D-printed models in Main Text Figs. 2(f) and 4(b).

To reduce the computational cost, in most of our analyses, we took advantage of the periodicity of the structures and investigated their response using the unit cells shown in Supplementary Fig. 6. To subject the unit cells to a macroscopic deformation gradient $\overline{\mathbf{F}}$ periodic boundary conditions were imposed on all cell boundaries by enforcing[S9,S10]

$$\mathbf{u}_\alpha^{A_i} - \mathbf{u}_\alpha^{B_i} = (\overline{\mathbf{F}}_{\alpha\beta} - \delta_{\alpha\beta})(\mathbf{X}_\beta^{A_i} - \mathbf{X}_\beta^{B_i}), \quad i = 1, 2, ..., K \tag{37}$$

where $\delta_{\alpha\beta}$ is the Kronecker delta, $\mathbf{u}_\alpha^{A_i}$ and $\mathbf{u}_\alpha^{B_i}$ ($\alpha = 1, 2$) are displacements of points periodically located on the boundary of the unit cell. Moreover, $\mathbf{X}_\alpha^{A_i}$ and $\mathbf{X}_\alpha^{B_i}$ ($\alpha = 1, 2$) are the initial coordinates of points periodically located on the boundary of the unit cell and K denotes the number of pairs of nodes periodically located on the boundary of the unit cell. Note that the components of $\overline{\mathbf{F}}$ can be conveniently prescribed within the finite element framework using a set of virtual nodes. The corresponding macroscopic first Piola-Kirchoff stress is then obtained through virtual work considerations[S9,S10]. To subject the structures to uniaxial compression, we prescribed

$$\overline{\mathbf{F}} = \begin{bmatrix} \text{UNSET} & 0 \\ 0 & 1 + \varepsilon_y \end{bmatrix}, \tag{38}$$

where ε_y is the macroscopic applied strain. Moreover, in order to investigate the structure's response for different loading directions, we rotated the unit cell model by an angle θ and re-applied the above periodic boundary conditions using the rotated geometry coordinates. To determine the linear stiffness for the infinite structures we performed a small strain linear elastic analysis. For all buckling analyses, we performed a linear stability buckling analysis (`*Buckling` command in ABAQUS input file). Since buckling may alter the periodicity of the structure, we considered super cells consisting of $M \times M$ undeformed RVEs with $M \in [1, 10]$ subjected to periodic boundary conditions and calculated the critical strain for each of them. The critical strain of the infinite periodic structure was subsequently defined as the minimum critical strain on all considered super cells. The results reported in Supplementary Fig. 7 show that for *Design A-C* the critical strain is identical for all considered values of M, indicating that the structure undergoes a local (microscopic) instability with wavelength corresponding to the size of the RVE. *Design D*, on the other hand, undergoes a global (macroscopic) instability, as the minimum critical strain is observed for $M = 10$ (Supplementary Fig. 8).

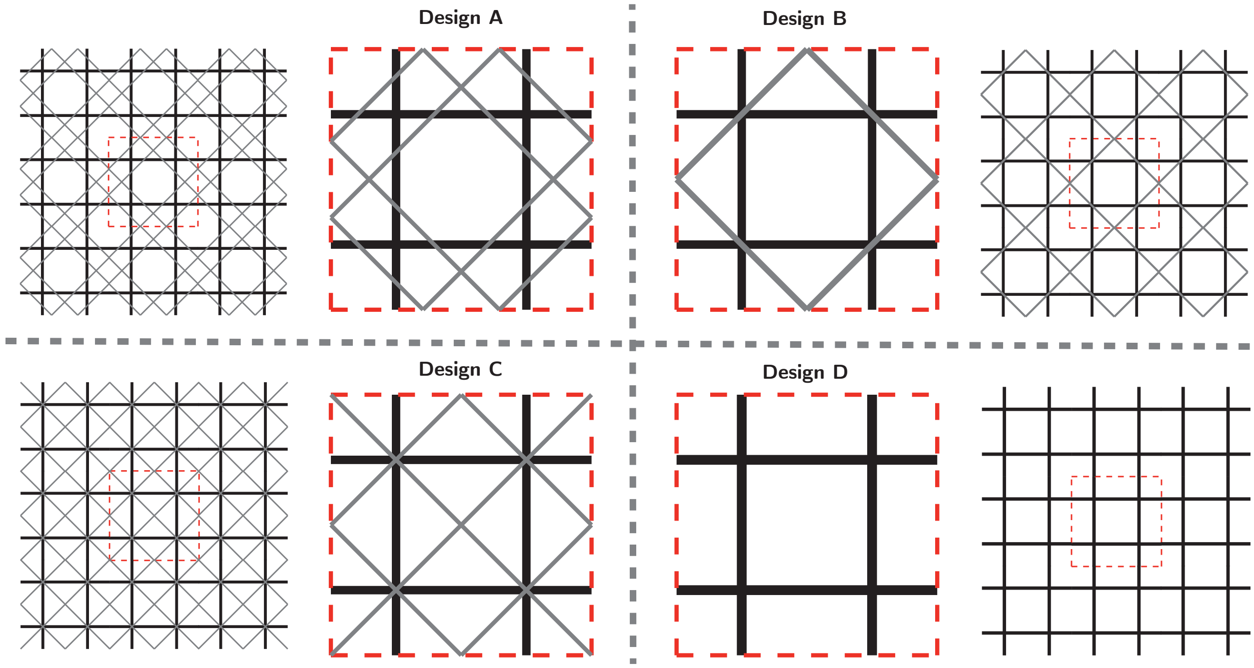

Supplementary Figure 6: **RVE used for the different designs.** Schematics of the RVEs used for *Design A-D*. Periodic boundary conditions are applied on the nodes that intersect with the red dashed line.

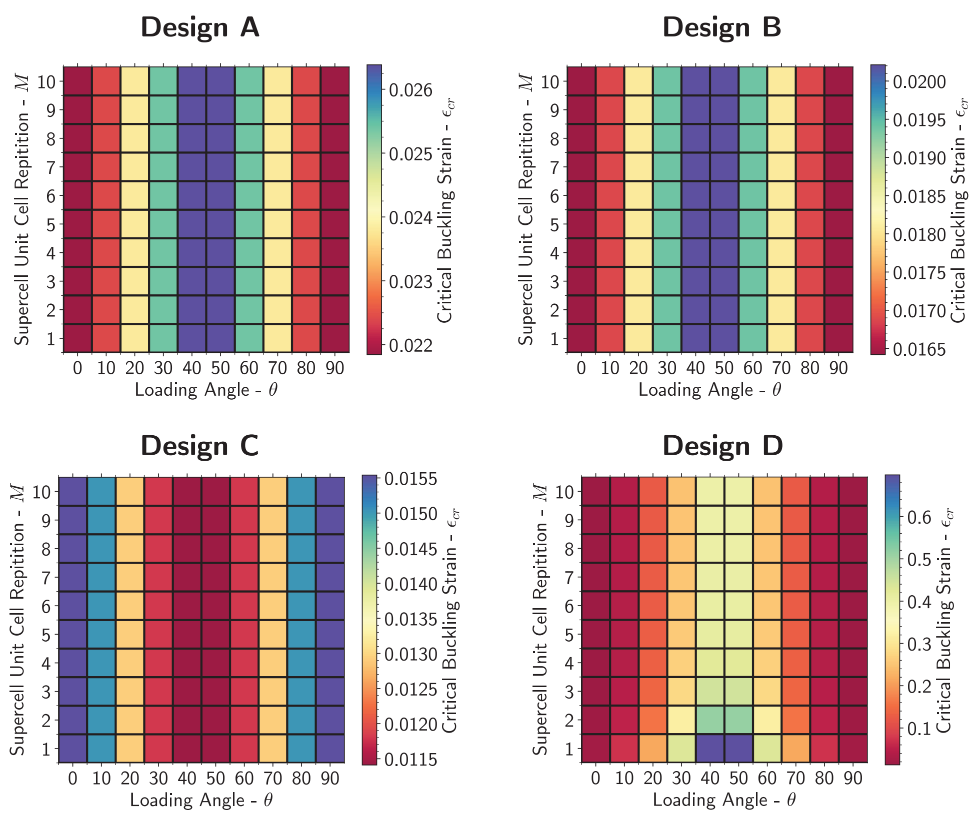

Supplementary Figure 7: **Global versus local instabilities.** In each contour plot, we report the critical strain as a function of θ and the size of the super cell. For each of the simulations, periodic boundary conditions are applied along the outer perimeter of the $M \times M$ structure. This plot conveys that for *Designs A-C* the prominent buckling mode is the local mode, whereas for *Design D*, the prominent mode is a global mode. Choosing a sufficiently large M allows *Design D* to converge to a finite value for each θ.

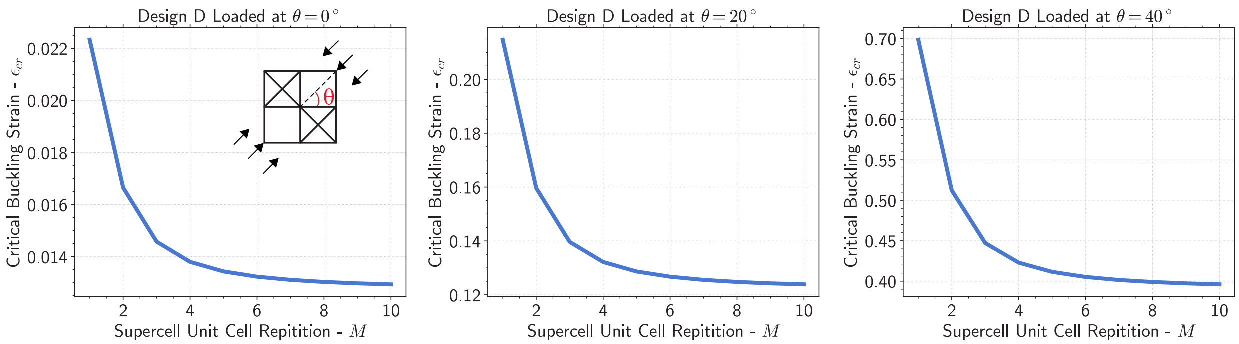

Supplementary Figure 8: **Critical strain for *Design D* at three selected loading angles.** As the number of minimum RVEs M considered increases, the value for the critical buckling strain asymptotically approaches a constant.

S4.1: Additional numerical results

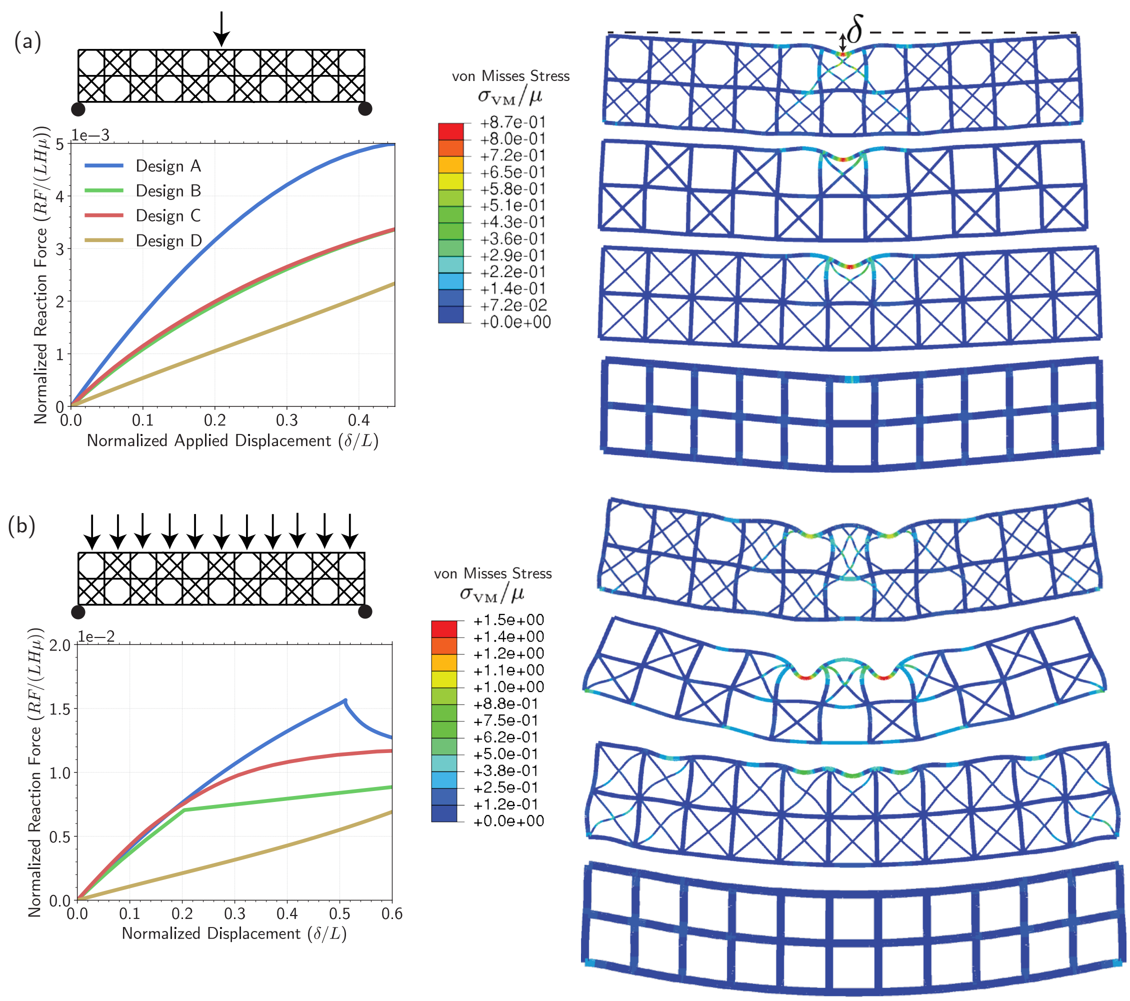

Supplementary Figure 9: **Mechanical response for different loading conditions.** For all cases presented in this figure, we consider a structure with 11×2 cells (5.5 RVEs) and hinged boundary conditions applied to cells *with* diagonal reinforcements. (a) In this case, a point deflection δ is applied to the top center of the structure while the bottom outside corners have constrained deflections, but unconstrained rotation. The normalized reaction force is plotted as a function of the δ for the four considered designs. Moreover, on the right we show numerical snapshots of the four designs for $\delta/L = 0.45$. The colors in these pictures provide a measure of the normalized von Mises stress. (b) In this case a distributed load is applied across the top of the structure while the bottom outside corners have constrained displacements, but unconstrained rotation. The normalized total reaction force is plotted as a function of the deflection for the four considered designs. On the right we show numerical snapshots of the four designs for $\delta/L = 0.6$, where δ is the vertical deflection of the top mid-point from the undeformed configuration. The colors in these pictures provide a measure of the normalized von Mises stress.

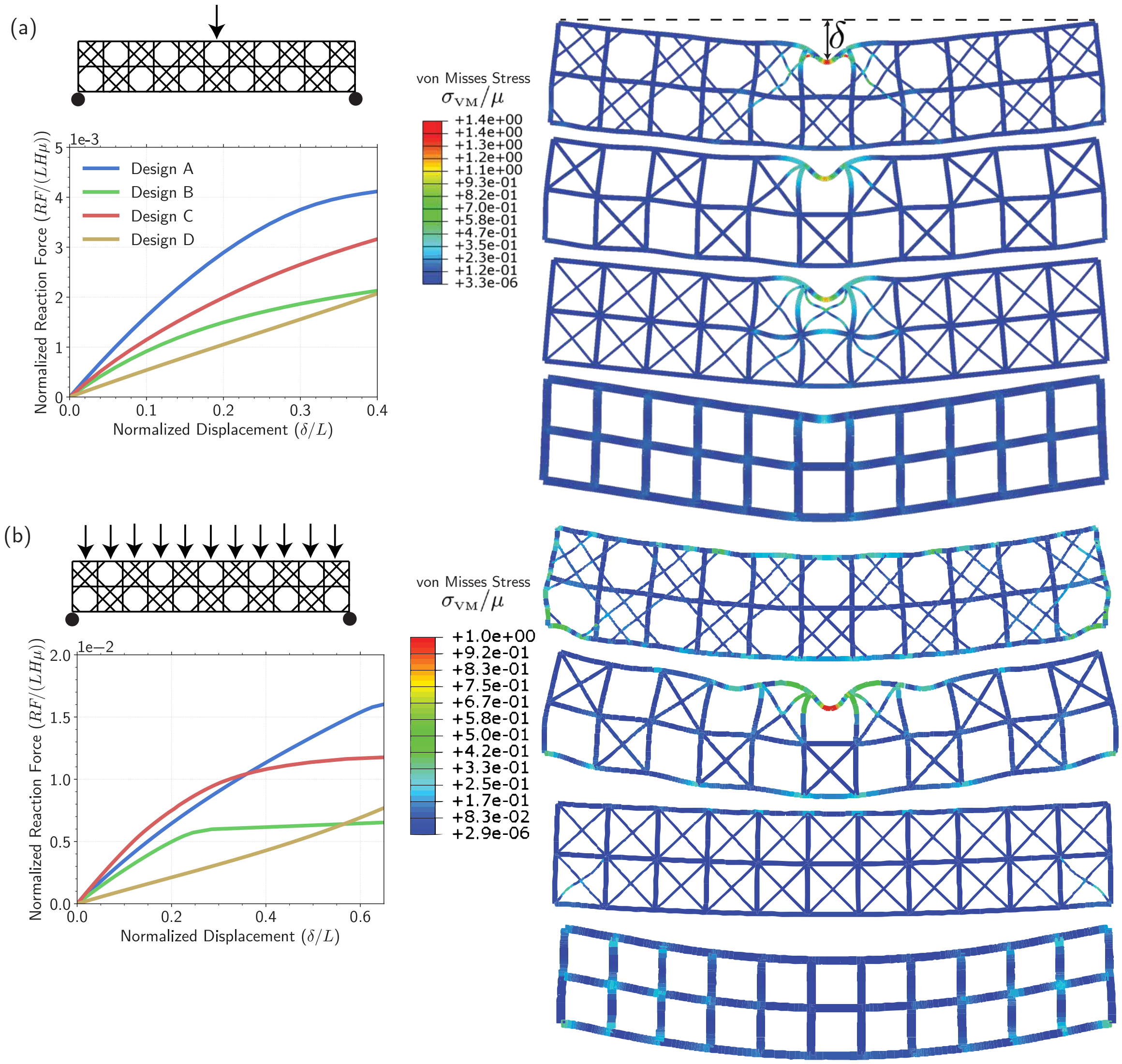

Supplementary Figure 10: Mechanical response for different loading conditions. For all cases presented in this figure, we consider a structure with 11×2 cells (5.5 RVEs) and hinged boundary conditions applied to cells *without* diagonal reinforcements. (a) In this case, a point deflection δ is applied to the top center of the structure while the bottom outside corners have constrained deflections, but unconstrained rotation. The normalized reaction force is plotted as a function of the δ for the four considered designs. Moreover, on the right we show numerical snapshots of the four designs for $\delta/L = 0.45$. The colors in these pictures provide a measure of the normalized von Mises stress. (b) In this case a distributed load is applied across the top of the structure while the bottom outside corners have constrained displacements, but unconstrained rotation. The normalized total reaction force is plotted as a function of the deflection for the four considered designs. On the right we show numerical snapshots of the four designs for $\delta/L = 0.6$, where δ is the vertical deflection of the top mid-point from the undeformed configuration. The colors in these pictures provide a measure of the normalized von Mises stress.

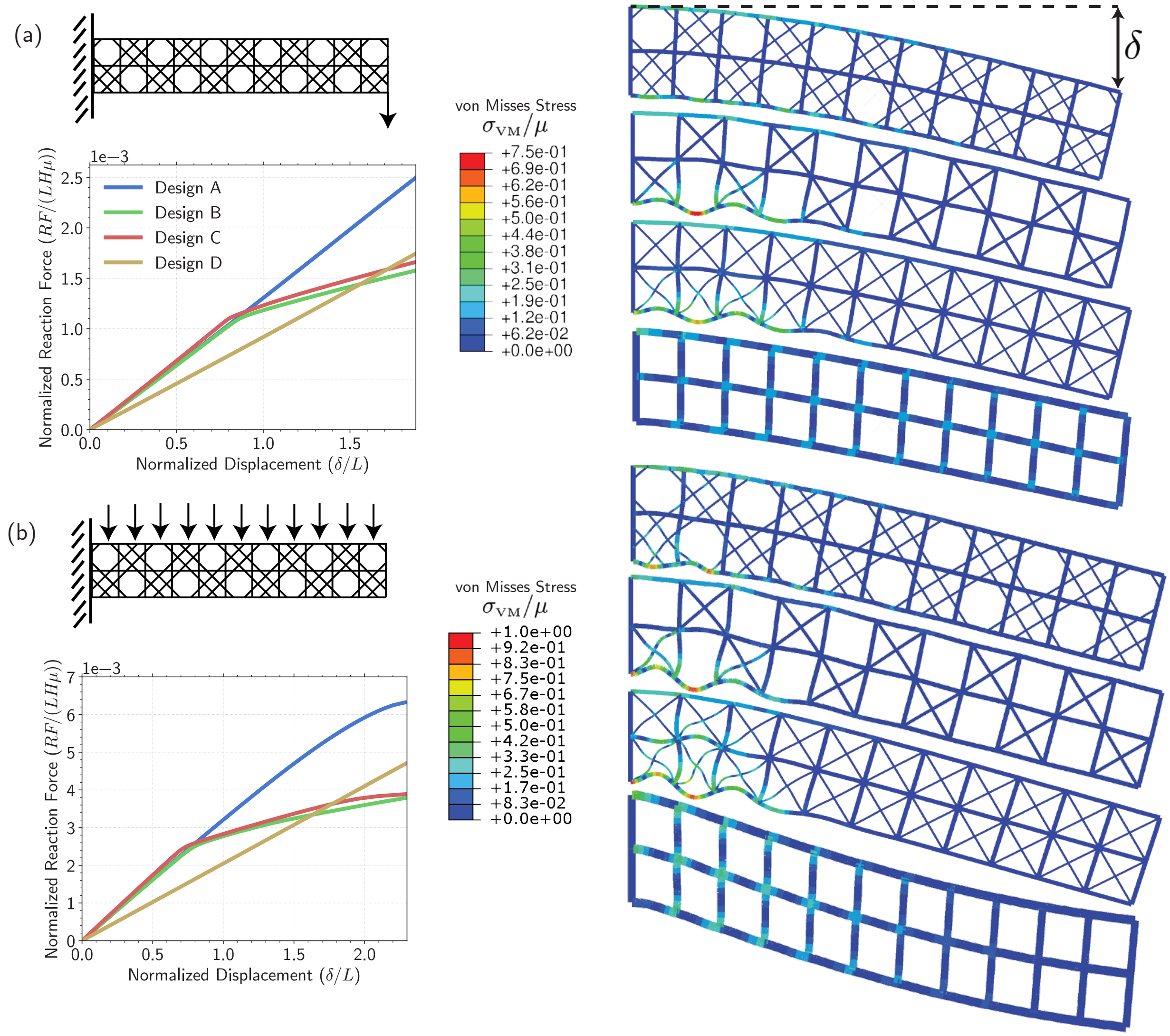

Supplementary Figure 11: Mechanical response for different loading conditions. For all cases presented in this figure, we consider a long slender realization of each design consisting of 11×2 cells (5.5 RVEs). (a) In this case, a point deflection δ is applied to the bottom right of the structure while the left edge of the structure is fixed. The normalized total reaction force is plotted as a function of the deflection for the four considered designs. Moreover, on the right we show numerical snapshots of the four designs for $\delta/L = 1.9$. The colors in these pictures provide a measure of the normalized von Misses stress. (b) In this case a distributed load is applied across the top of the structure while the left edge of the structure is fixed. The normalized total reaction force is plotted as a function of the deflection for the four considered designs. On the right we show numerical snapshots of the four designs for $\delta/L = 2.3$, where δ is the vertical deflection of the top right edge-point from the undeformed configuration. The colors in these pictures provide a measure of the normalized von Mises stress.

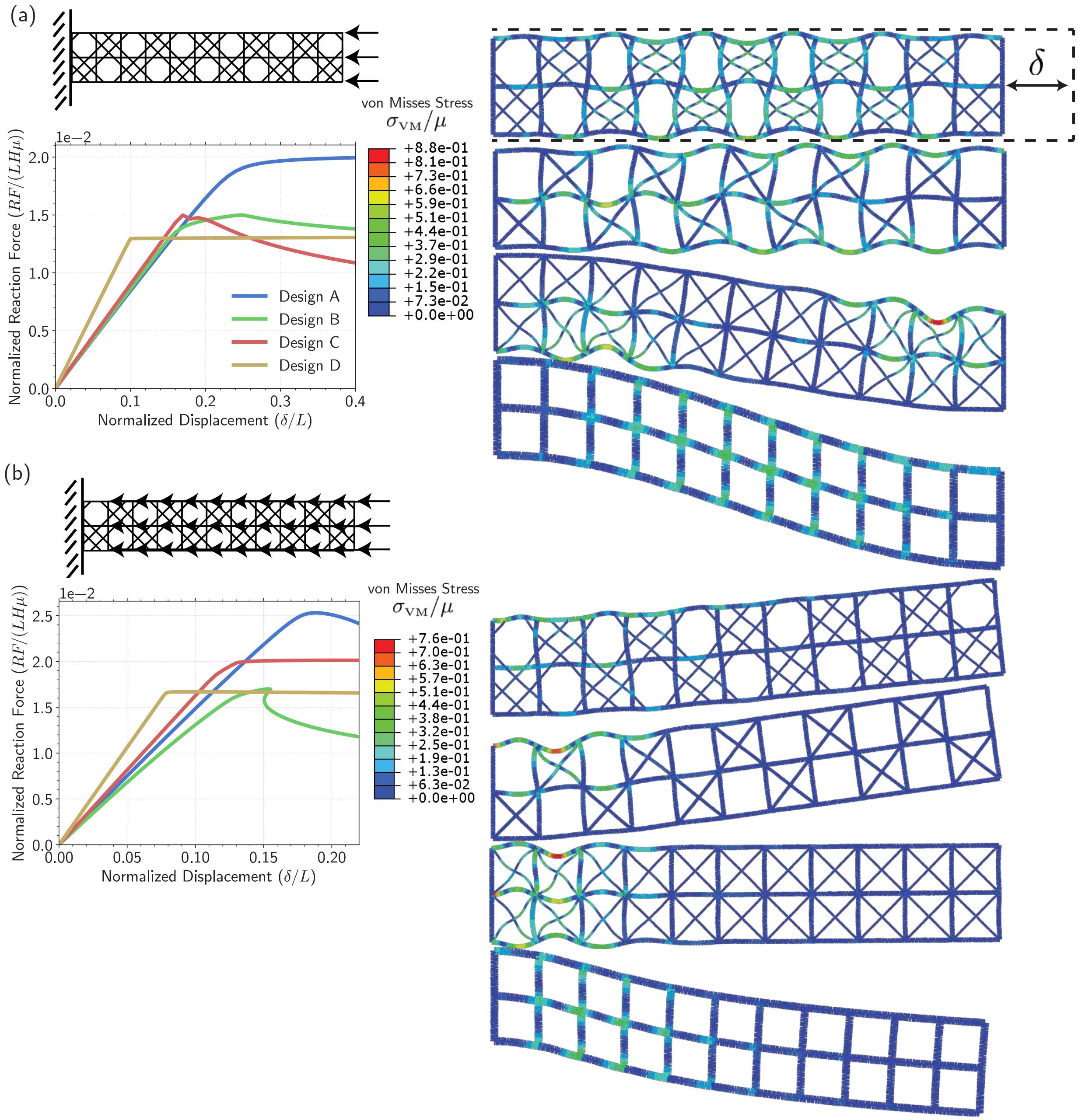

Supplementary Figure 12: Mechanical response for different loading conditions. For all cases presented in this figure, we consider a long slender realization of each design consisting of 11×2 cells (5.5 RVEs). (a) In this case a deflection δ is applied to the right edge of the structure while the left edge of the structure is fixed. The normalized total reaction force is plotted as a function of the applied deflection for the four considered designs. Moreover, on the right we show numerical snapshots of the four designs for $\delta/L = 0.4$. The colors in these pictures provide a measure of the normalized von Misses stress. (b) In this case a distributed load is applied across each level of the structure while the left edge of the structure is fixed. The normalized total reaction force is plotted as a function of the deflection for the four considered designs. On the right we show numerical snapshots of the four designs for $\delta/L = 0.22$, where δ is the horizontal deflection of the right mid-point from the undeformed configuration. The colors in these pictures provide a measure of the normalized von Mises stress.

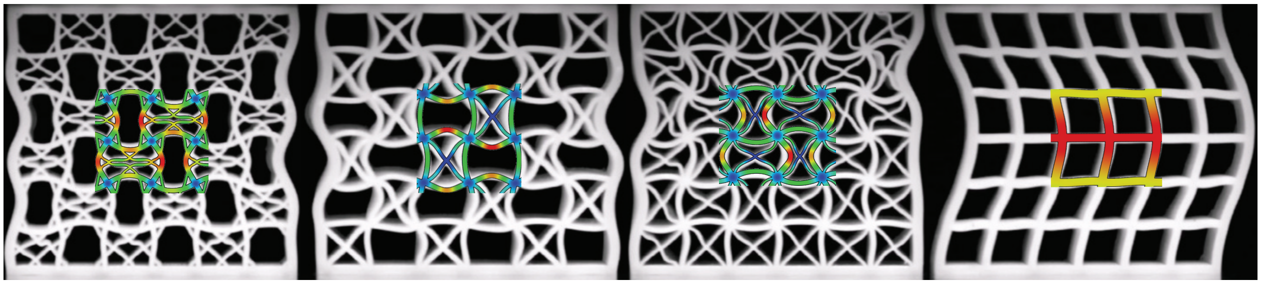

Supplementary Figure 13: Comparison between experimental and numerical results. This figure shows experimental snapshots of the experimental specimens at an applied 8% compressive strain overlaid with a cutout of the representative deformation predicted by our FE analyses. The close agreement between the experiments and simulations suggests that the FE simulations are accurately capturing the physical deformation of the specimens.

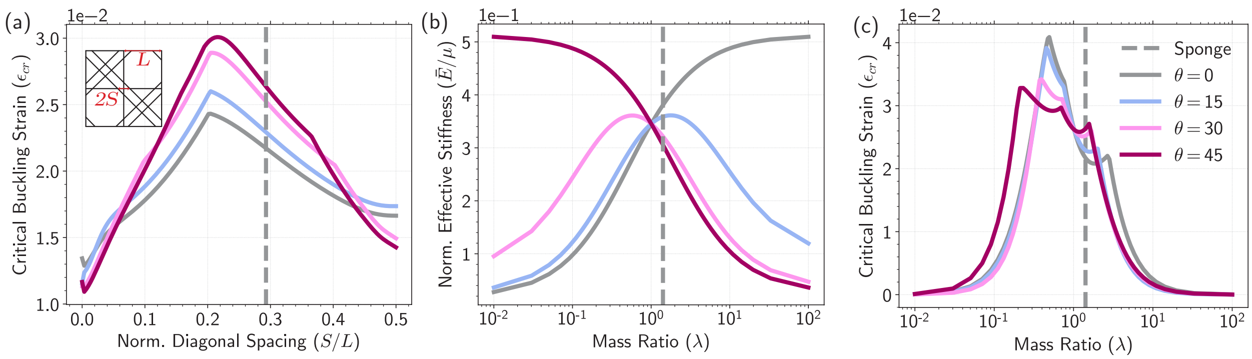

Supplementary Figure 14: Effect of diagonal spacing and mass ratio on the response of *Design A* with rectangular cross-section. (a) Evolution of the critical strain as function of the spacing between diagonals. (b) Evolution of structural stiffness as a function of the mass ratio $\lambda = V_{nd}/V_d$. (c) Evolution of critical strain as a function of the mass ratio λ. For each of the plots, the gray dashed vertical line indicates the parameter of *Design A*. These results demonstrate that *Design A*, the sponge design, is very close to the optimal one, when considering each parameter individually. All designs are characterized by the same total volume.

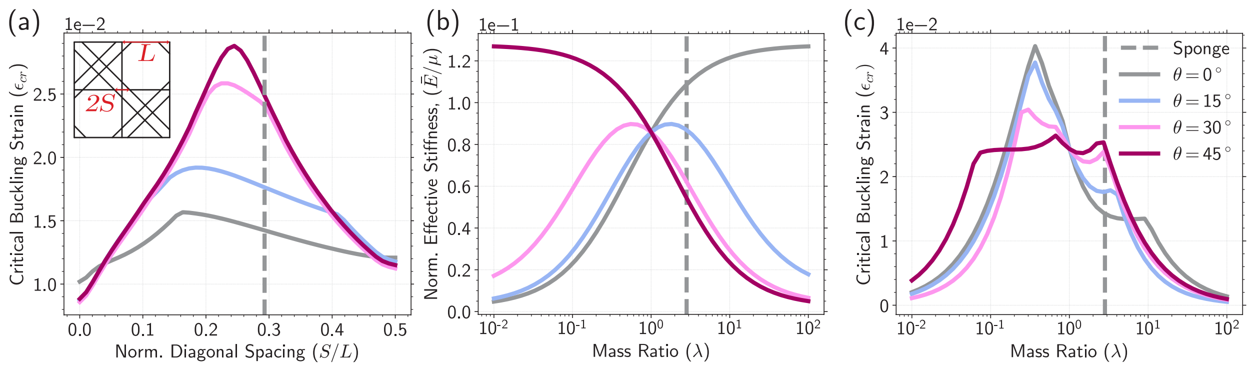

Supplementary Figure 15: Effect of diagonal spacing and mass ratio on the response of *Design A* with circular cross-section. (a) Evolution of critical strain as function of the spacing between diagonals. (b) Evolution of structural stiffness as a function of the mass ratio $\lambda = V_{nd}/V_d$. (c) Evolution of critical strain as a function of the mass ratio λ. For each of the plots, the gray dashed vertical line indicates the parameter of *Design A*. These results demonstrate that the shape of the cross-section does not have a significant role, as these results are similar to those presented in Supplementary Fig. 14 for a lattice with rectangular cross-section. All designs are characterized by the same total volume.

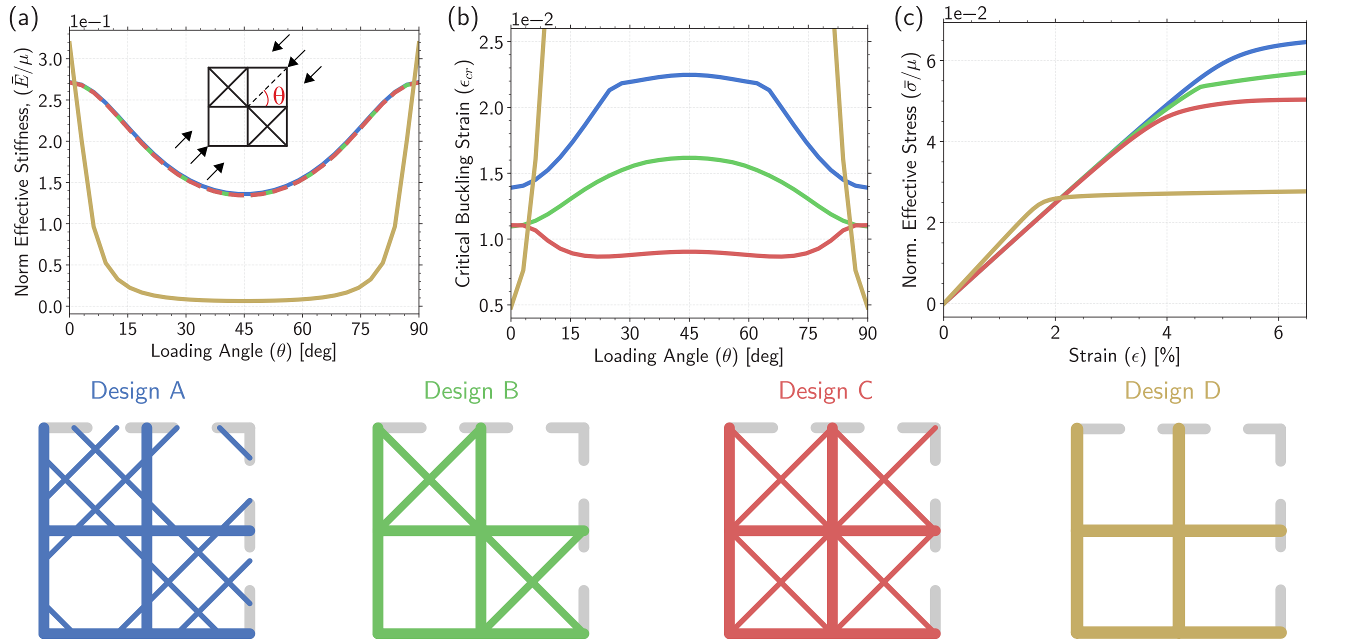

Supplementary Figure 16: **Response of *Design A-D* with circular cross-section.** (a) Evolution of the structural stiffness as a function of loading angle θ for lattices of infinite size. (b) Evolution of the effective buckling stress for the different lattice designs as a function of loading angle θ. Results are obtained by simulating a super-cell with 10 by 10 units and periodic boundary conditions. (c) Numerically predicted stress-strain curves for the 4 considered lattices when compressed with $\theta = 0$. For all plots, the color of the line corresponds to the respective design color depicted on the bottom.

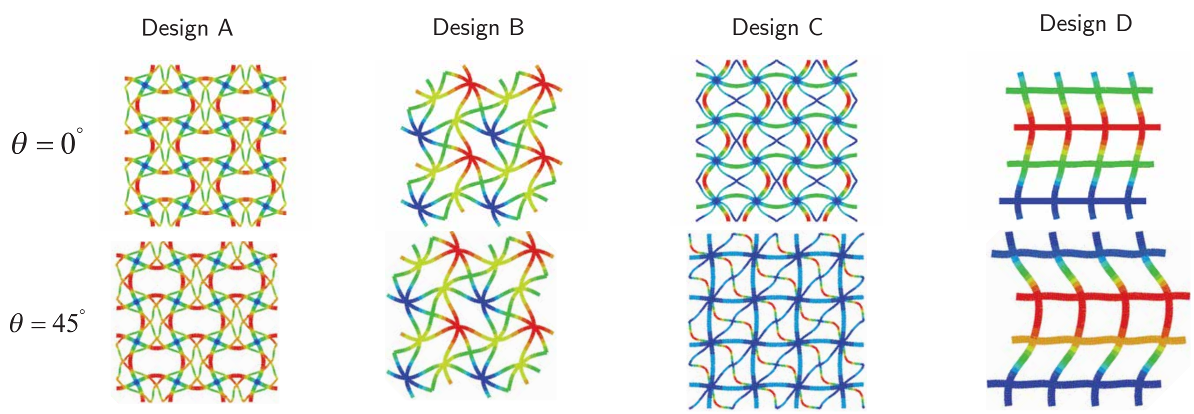

Supplementary Figure 17: **Critical modes of *Design A-D* at $\theta = 0^\circ$ and $\theta = 45^\circ$.** These critical buckling modes were calculated using a 10 by 10 super-cell and the snapshots shown here are the center 2x2 cells of the full 10x10 model. *Designs A-B* in this figure exhibit a similar deformation pattern when loaded at 0° or 45°. However, for *Design C-D*, different buckling patterns are triggered when loaded at 0° and 45°.

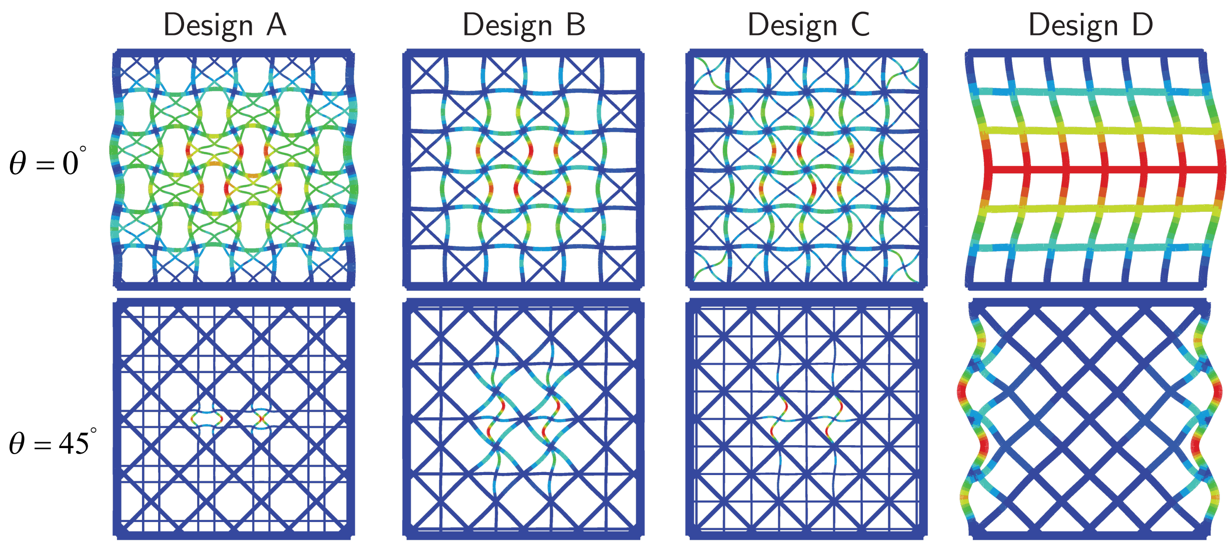

Supplementary Figure 18: Modes of finite size structure comprised of 3x3 unit cells. This figure shows the critical buckling modes obtained for finite geometries for *Design A-D* loaded in uniaxial compression. The top row corresponds to a structure angled at 0°, as in the experiments. The second row corresponds to the same structure however rotated by 45° and cut to maintain the same size as the row above. Each column in this figure corresponds to a different design. For each of the geometries, a slightly thicker frame is constructed to localize most of deformation away from the edges of the structure. These results convey that the diagonally reinforced geometries are not susceptible to edge effects when using at least 3 unit cells, whereas the non-diagonally reinforced structure is more susceptible to edge effects.

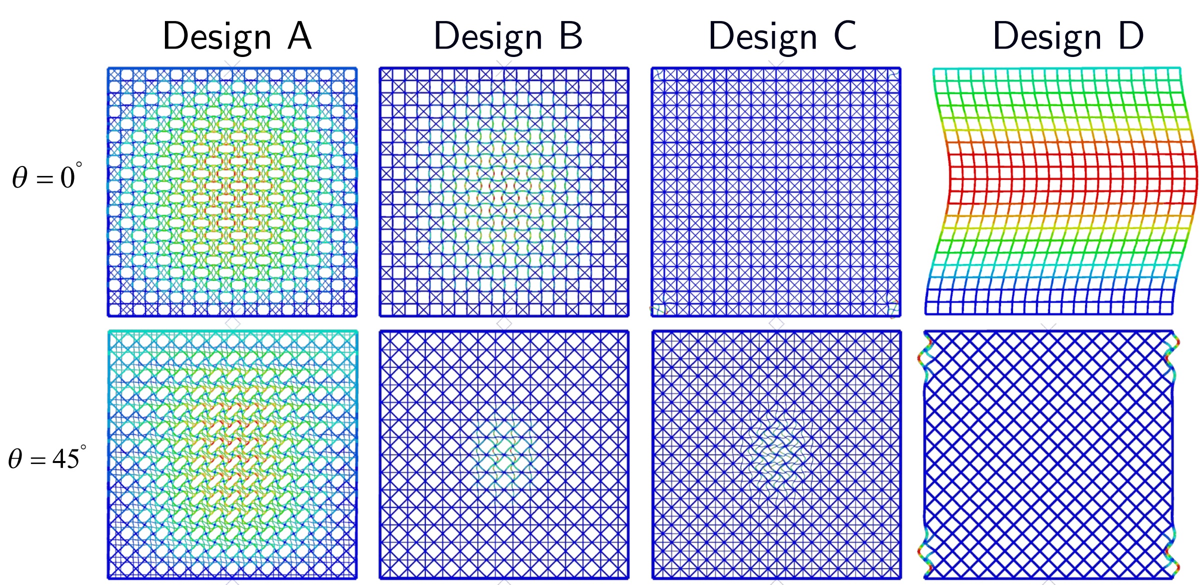

Supplementary Figure 19: Modes of finite size structure comprised of 10x10 unit cells. This figure shows the critical buckling modes obtained for finite geometries of *Design A-D* loaded in uniaxial compression. The top row corresponds to a structure angled at 0°, as considered in the experiments. The second row corresponds to the same structure however rotated by 45° and cut to maintain the same size as the row above. Each column in this figure corresponds to a different design. For each of the geometries, a slightly wider frame is constructed to minimize edge effects.

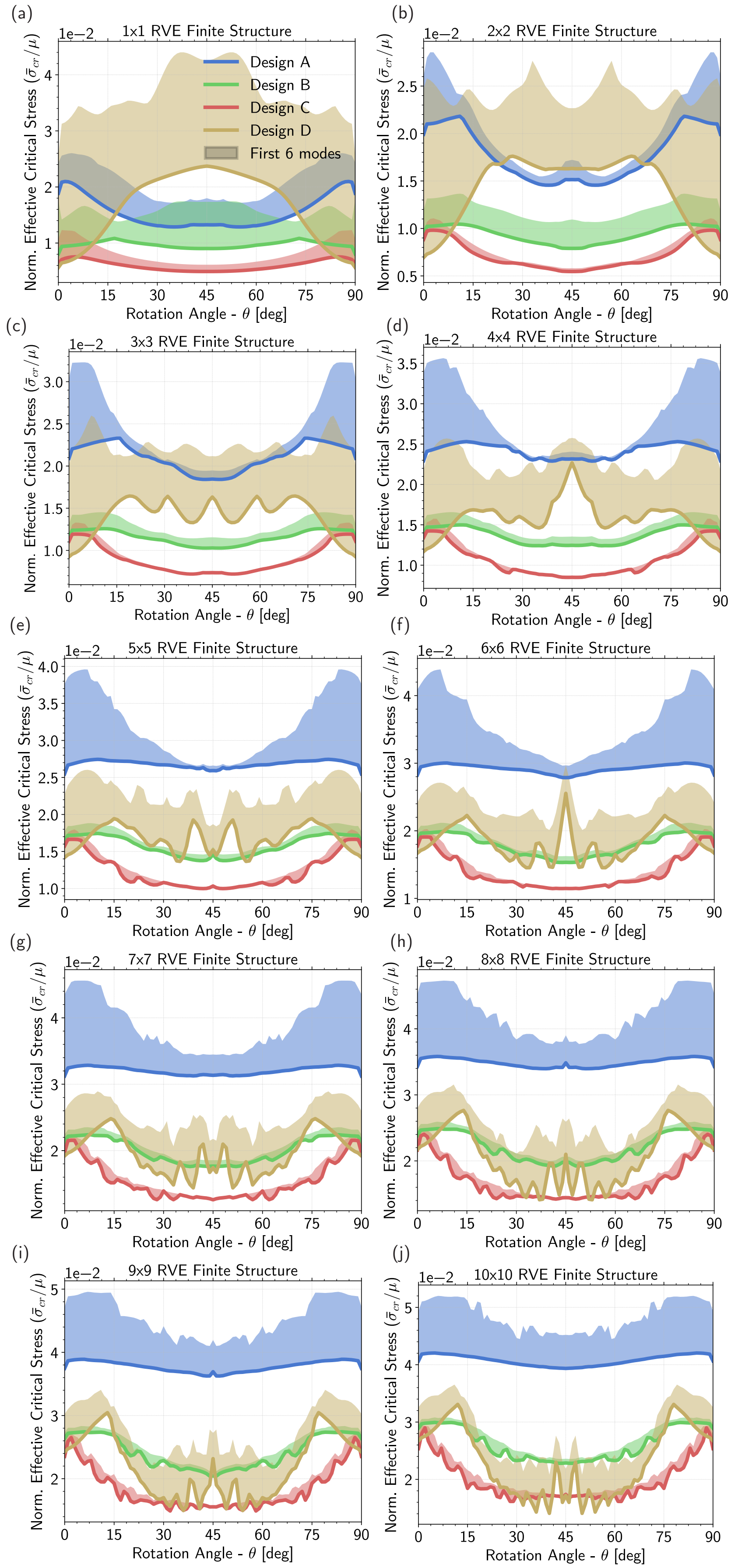

Supplementary Figure 20: Effect of sample size on critical stress. Evolution of the effective buckling stress as a function of the loading angle θ for finite-size lattice structures comprising M by M unit cells, where M ranges from (a) 1 to (j) 10. The shaded parts in (a) - (j) represent the lowest six buckling modes range. All plots provide a clear indication on the superior performance of *Design A* when comparing to *Designs C-D*, when $M > 2$.

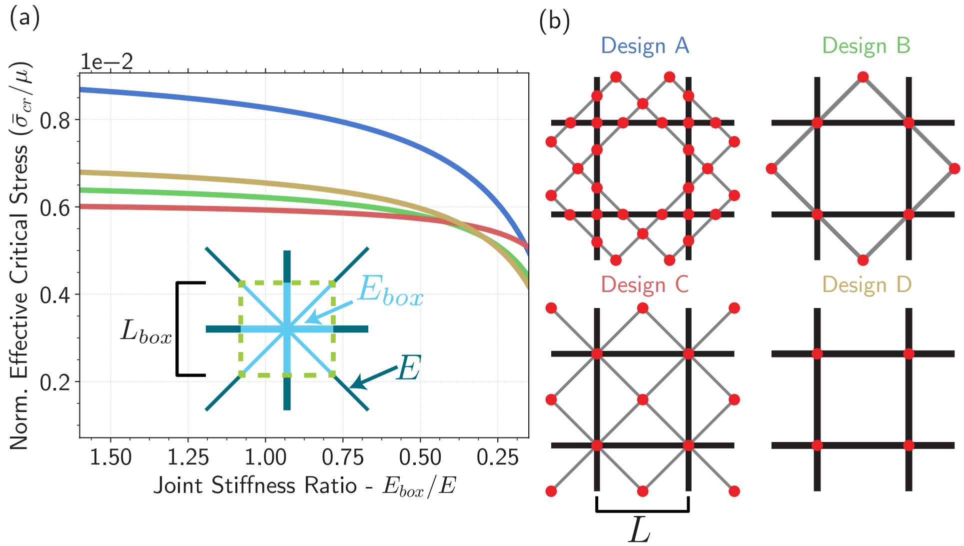

Supplementary Figure 21: **Effect of joint stiffness analysis on critical stress.** To evaluate the influence of the joints on the effective buckling stress of *Designs A-D* we conduct FE analysis on a period unit cell with modified stiffness on elements near the joints. In particular, we set the material stiffness to E_{box} for the elements within a box of edge length $L_{box} = 0.02L$ (see inset schematic in (a)). (a) Evolution of the normalized effective critical stress for varying the joint stiffness ratio E_{box}/E. (b) Schematic of *Design A-D* unit cells with the location of the joints highlighted by red dots.

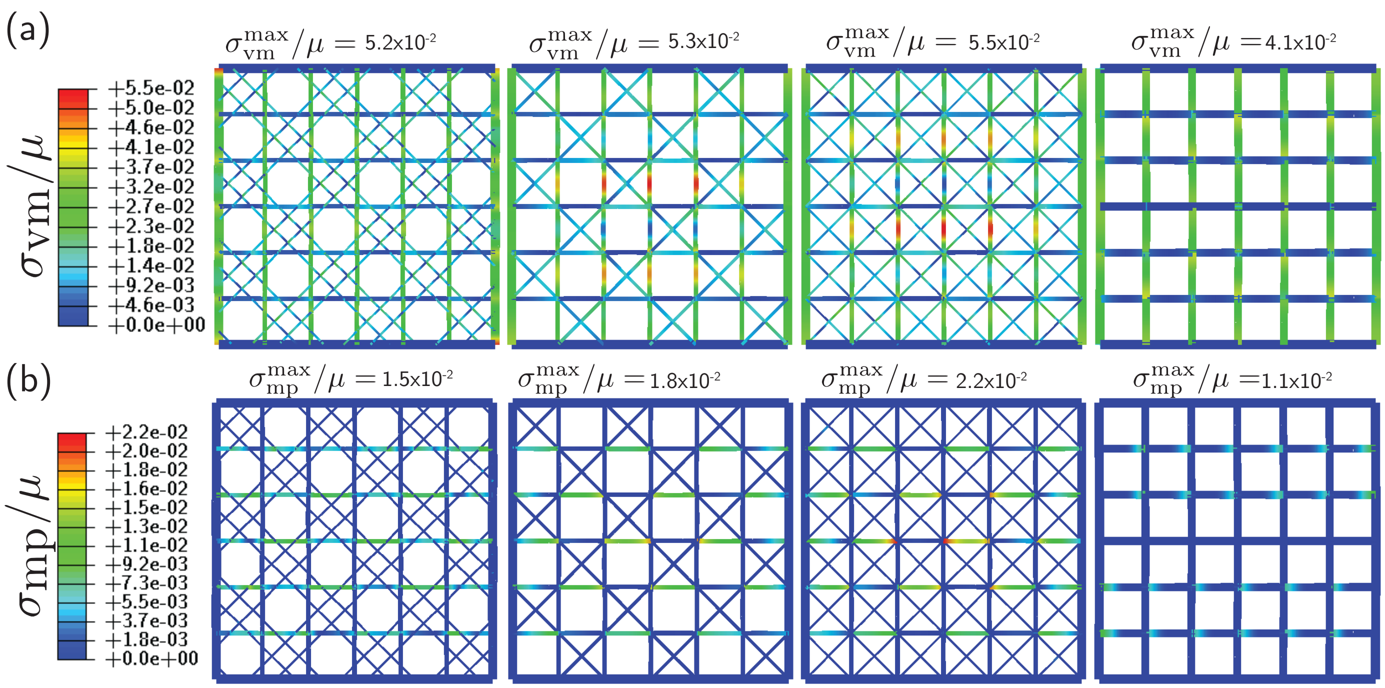

Supplementary Figure 22: **Stress Analysis.** Numerical snapshots extracted from non-linear FE analysis (with first mode imposed imperfection) at an imposed strain $\epsilon = 0.001$. (a) The color indicates the normalized von Mises stress σ_{vm} with the maximum value for each structure indicated above each figure. (b) The color indicates the normalized maximum principle stress σ_{mp} with the maximum value for each structure indicated above each figure.

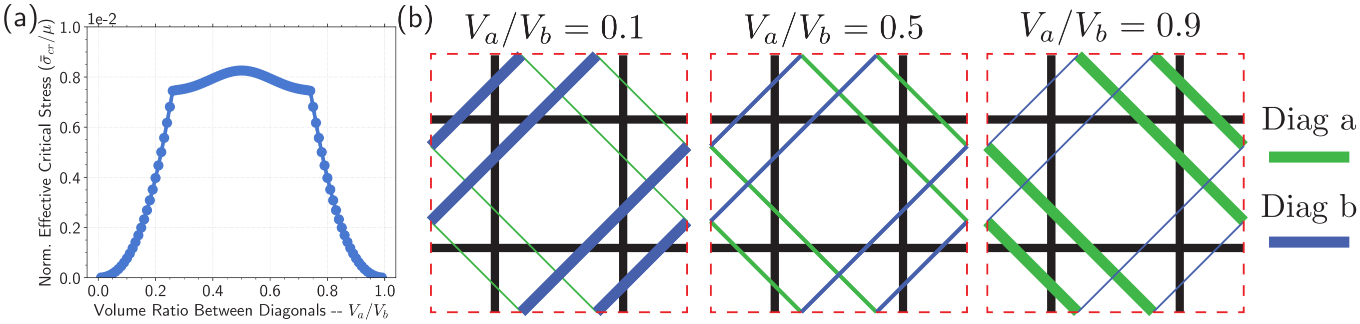

Supplementary Figure 23: Effect of disorder on critical stress. To evaluate the influence of disorder on the effective buckling stress of *Design A*, we conduct FE analysis on a period unit cell on which we vary the mass allocated between diagonals going in different directions. For all analysis presented, the total volume allocated between diagonals and non-diagonals remains constant, namely $\lambda = \sqrt{2}$. V_a/V_b defines the ratio between the volume allocated to the two families of diagonals (with $V_a + V_b = V_{nd}/\sqrt{2}$). (a) Evolution of the effective buckling stress as a function of V_a/V_b for $\theta = 0$. We find that for $0.25 < V_a/V_b < 0.75$ disorder has a minor effect on the effective buckling stress. (b) Schematics of selected unit cell with different diagonal volume allocations V_a/V_b.

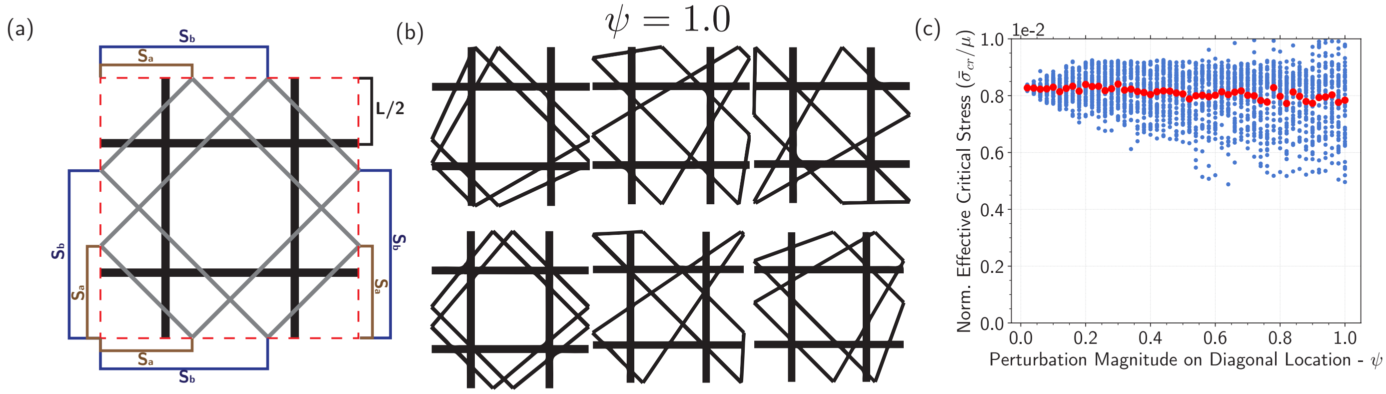

Supplementary Figure 24: Effect of disorder on critical stress. To evaluate the influence of disorder on the effective buckling stress of *Design A* we conduct FE simulations on a periodic unit cell in which we vary the location and orientation of individual diagonals, while maintaining periodicity of the structure. For all analysis presented, the total volume of the diagonals remains constant and equal to $V_{nd}/\sqrt{2}$. (a) Schematic illustrating the spacing S_a and S_b, defining the position of each diagonal. (b) Schematics of unit cell with varying S_a and S_b (with $S_a, S_b \in [0, 2L]$). (c) Effective buckling stress for 2,500 unit cell simulations, in which we perturb the sponge strut spacings S_a and S_b using a Gaussian $\mathcal{N}$ with mean $\mu = 0$, standard deviation $\sigma = 0.3$ and magnitude ψ, namely, $S_a/L = 1 - 1/(\sqrt{2}+2) + \psi\mathcal{N}(0, 0.3)$ and $S_b/L = 1 + 1/(\sqrt{2}+2) + \psi\mathcal{N}(0, 0.3)$. The red markers indicate the mean for each considered ψ containing $n = 50$ simulations per discrete value of ψ. We find that the applied perturbation does not alter the mean effective critical stress and that the variation of $\bar{\sigma}_{cr}$ is bounded between $0.6 \times 10^{-2}\mu$ and $1.0 \times 10^{-2}\mu$.

S5: OPTIMIZATION ANALYSIS

In an effort to identify the diagonal reinforcement resulting in a square lattice with the highest critical load, we used a Python implementation of the Covariance Matrix Adaptation Evolution Strategy (CMA-ES)[S11]. CMA-ES is an evolutionary algorithm that is used to solve optimization problems by iteratively solving several forward problems to adjust a covariance matrix of the solution. Since it is a derivative free algorithm, CMA-ES is well suited for optimization problems of high dimensionality and non-linear parameter topology. In this study we used CMA-ES to identify

- the number of diagonals, N
- the volume ratio of non-diagonal to diagonal members, $\lambda = V_{nd}/V_d$. Note that, since for a lattice with N diagonal members

$$V_{nd} = 8T_{nd}LH, \tag{39}$$

$$V_d = 4\sqrt{2}NT_dLH, \tag{40}$$

for a given λ T_{nd} and T_d are given by

$$T_{nd} = \frac{1}{2}\frac{\lambda}{1+\lambda}\left(0.2L + 0.1\sqrt{2}L\right), \tag{41}$$

$$T_d = \frac{1}{\sqrt{2}}\frac{1}{N(1+\lambda)}\left(0.2L + 0.1\sqrt{2}L\right), \tag{42}$$

where we have enforced Eq. (1) and Eq. (9).

- the separation between each even set of diagonals, S_i for $i \in [1, 7]$ (Supplementary Fig. 25)

resulting in a lattice structure with the largest critical load. For such an optimization problem, the number of optimization variables increased with the number of diagonals incorporated in the model (i.e. the total number of parameters are $1 + \frac{1}{2}(N - (N \bmod 2))$ for a given optimization instance with N number of diagonals). In all of the runs we assumed that all diagonals are oriented at 45° with respect to the non-diagonal members and that V_d and V_{nd} were distributed equally among the diagonal and non-diagonal elements, respectively. Furthermore, to ensure the symmetry, we assumed that $S_{2i-1} = S_{2i}$ $(i = 1, 2, ..., N/2)$ if N is an even number and $S_1 = 0$ and $S_{2i-1} = S_{2i}$ $(i = 2, 3, ..., (N-1)/2)$ for odd values of N (Supplementary Fig. 25).

The algorithm's initial values were chosen to be in the center of the design space, namely, $\lambda = 1$ and diagonal separation for the even set of diagonals $S_i = 0.5L$. The covariance matrix was initialized uniformly with a standard deviation half of the domain space, which was normalized and constrained to remain between 0 and 1. The optimization was evaluated in a uniaxial loading condition aligned parallel to the vertical elements with a population size of 30.

For the optimization results presented in the Main Text, we sought to maximize the critical buckling load of a finite size structure using a single objective target function. The resultant parameter values from the optimization can be found in Supplementary Tab. 2 and a convergence analysis for the case of $N = 2$ can be found in Supplementary Fig. 26. Note that we also performed the same optimization analysis on an infinite periodic structure and the obtained results are shown in Supplementary Fig. 27, and Supplementary Tab. 3.

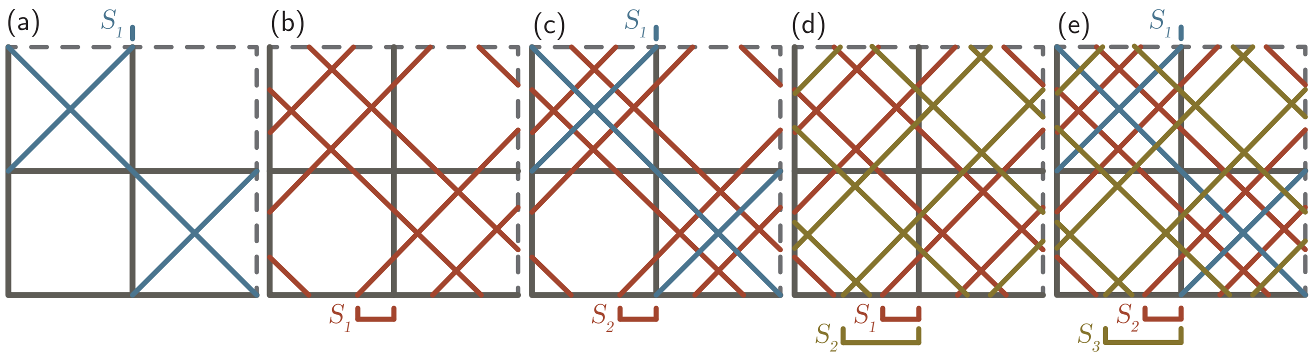

Supplementary Figure 25: Schematic. Schematics highlighting the geometric parameters considered in our optimization analysis.

	λ	S_1	S_2	S_3	S_4
$N=1$	3.1890	0			
$N=2$	0.6778	0.1800			
$N=3$	0.8028	0	0.3044		
$N=4$	0.7640	0.1912	0.3720		
$N=5$	0.3874	0	0.3881	0.7811	
$N=6$	0.5036	0.1910	0.5189	0.8712	
$N=7$	0.3561	0	0.2899	0.5512	0.8779

Supplementary Table 2: Optimal 3×3 finite-sized structures. Geometric parameters defining the 3×3 structures with highest critical stress identified by CMA-ES for different numbers of diagonals. In each row we report the optimal parameter identified for a given number of diagonals N. For odd N, S_1 is constrained to 0, meaning it is not allowed to move from the non-diagonal elements junction. As the number of diagonals is increased λ decreases, indicating that the algorithm allocates more mass to the diagonal elements.

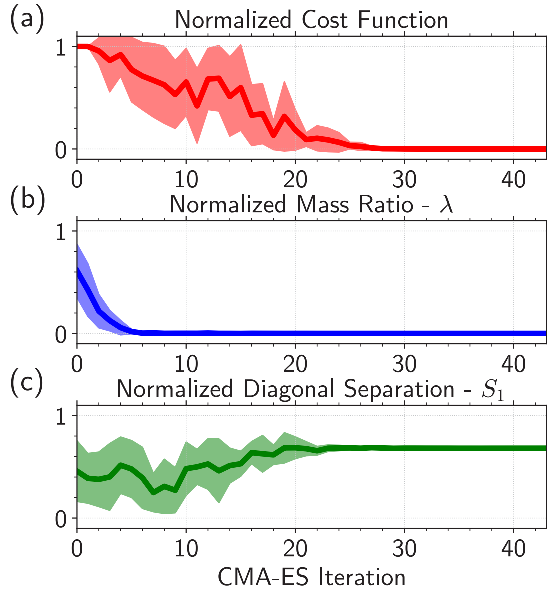

Supplementary Figure 26: Evolution of the objective function and design parameters during CMA-ES iterations. This figure shows the evolution of (a) the cost function, (b) the normalized mass ratio λ, and (c) the normalized diagonal separation S_1 over the course of each iteration of the optimization analysis for a lattice with $N = 2$. The solid line represents the mean value for the evolutionary optimization iteration (with population size $n = 30$ samples per iteration) and the shaded bounds represent the standard deviation from the mean. In this figure, it is apparent that the optimal value for λ is quickly identified by the algorithm.

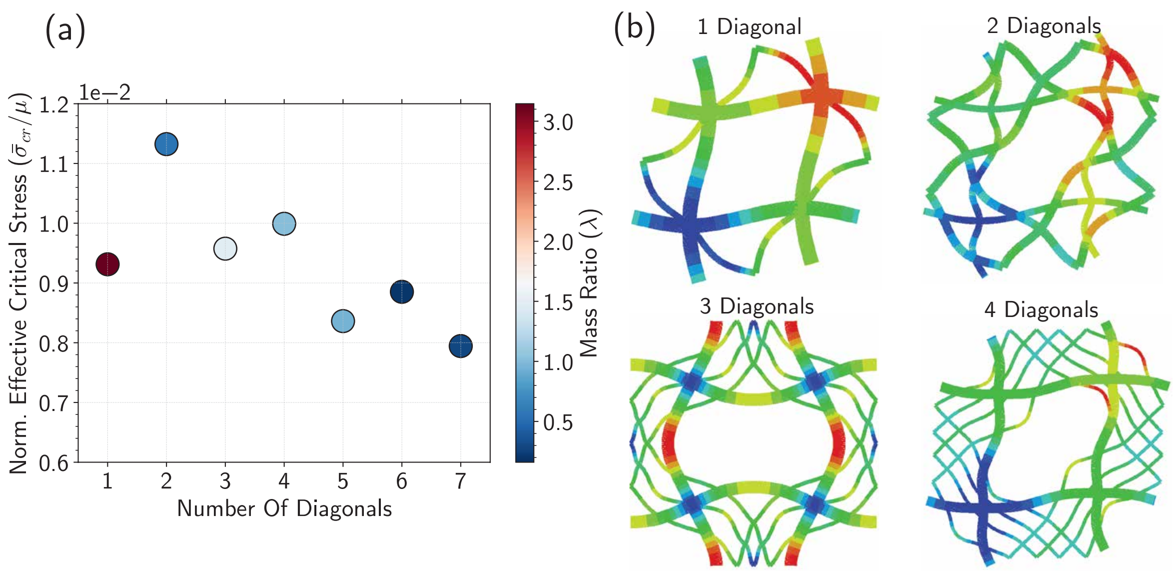

Supplementary Figure 27: Optimization analysis for infinite periodic structures. (a) Optimal value of critical buckling stress for varying number of diagonals. The color of each point represents the optimal mass ratio λ. (b) Optimal deformed geometries for designs including one to four diagonals. The color in each structure represents the magnitude of the displacement.

	λ	S_1	S_2	S_3	S_4
$N = 1$	3.1454	0			
$N = 2$	0.5614	0.3390			
$N = 3$	1.4784	0	0.2440		
$N = 4$	1.0151	0.0989	0.3358		
$N = 5$	0.9509	0	0.1733	0.3260	
$N = 6$	0.2009	0.2628	0.5827	0.8881	
$N = 7$	0.2962	0	0.4197	0.6917	0.9126

Supplementary Table 3: **Optimal structures of infinite extent**. Geometric parameters defining the infinite structures with highest critical stress identified by CMA-ES for different numbers of diagonals. Each column of the table corresponds to the optimal value of a parameter. Each row corresponds a determined N number of diagonals. For odd N, S_1 is constrained to 0, meaning it is not allowed to move from the non-diagonal elements junction. λ on average decreases as a function of N, which as expected, means the algorithm is allocating more volume to the diagonals as they are being spread too thin. The distribution of S as a function of N shows that the algorithm is attempting to evenly distribute the diagonal spacing, such that the length of the vertical elements without diagonal bracing is kept the shortest.

REFERENCES

[S1] Schulze, F. (1887). Report on the hexactinellida collected by hms" challenger" during the years 1873–1876. *HMS Challenger Sci Results Zool*, 21:1–513.

[S2] Schulze, F. (1904). *Hexactinellida, in Scientific Results of the German Deep-Sea Expedition with the Steamboat, Valdivia 1898–1899*. C. Chun (Ed.) Verlag Gustav Fischer, Jena, Germany.

[S3] Saito, T., Uchida, I., and Takeda, M. (2002). Skeletal growth of the deep-sea hexactinellid sponge euplectella oweni, and host selection by the symbiotic shrimp spongicola japonica (crustacea: Decapoda: Spongicolidae). *Journal of Zoology*, 258(4):521–529.

[S4] Aizenberg, J., Weaver, J. C., Thanawala, M. S., Sundar, V. C., Morse, D. E., and Fratzl, P. (2005). Skeleton of euplectella sp.: structural hierarchy from the nanoscale to the macroscale. *Science*, 309(5732):275–278.

[S5] Weaver, J. C., Aizenberg, J., Fantner, G. E., Kisailus, D., Woesz, A., Allen, P., Fields, K., Porter, M. J., Zok, F. W., Hansma, P. K., et al. (2007). Hierarchical assembly of the siliceous skeletal lattice of the hexactinellid sponge euplectella aspergillum. *Journal of structural biology*, 158(1):93–106.

[S6] Waddell, J. A. L. (1916). *Bridge engineering*, volume 1. J. Wiley.

[S7] Gibson, L. J. and Ashby, M. F. (1999). *Cellular solids: structure and properties*. Cambridge university press.

[S8] Deshpande, V., Ashby, M., and Fleck, N. (2001). Foam topology: bending versus stretching dominated architectures. *Acta Materialia*, 49(6):1035–1040.

[S9] Danielsson, M., Parks, D. M., and Boyce, M. C. (2002). Three-dimensional micromechanical modeling of voided polymeric materials. *Journal of Mechanics Physics of Solids*, 50:351–379.

[S10] Bertoldi, K. and Boyce, M. C. (2008). Mechanically triggered transformations of phononic band gaps in periodic elastomeric structures. *Phys. Rev. B*, 77:052105.

[S11] Hansen, N., Müller, S. D., and Koumoutsakos, P. (2003). Reducing the time complexity of the derandomized evolution strategy with covariance matrix adaptation (cma-es). *Evolutionary Computation*, 11(1):1–18.